Optimizing mechanical properties in single-layered and multi-layered amorphous carbon coatings

Sachin V. Muley [a, b, *], Aiping Zeng [c], Paul M. Voyles [a], Patrick J. Heaney [c, *]

[a] Department of Materials Science and Engineering, University of Wisconsin-Madison, 1509 University Avenue, Madison, WI 53706, United States of America

[b] Present address – Intel Corporation, 2501 NE Century Ave, Hillsboro, OR 97124, United States of America

[c] NCD Technologies, 510 Charmany Dr, Madison, WI 53719, United States of America

Author contact information:

Sachin Muley (sachinmul@gmail.com, +1 608-422-2165, corresponding author)

Aiping Zeng (aiping@ncdtechnologies.com)

Paul Voyles (paul.voyles@wisc.edu)

Patrick Heaney (patrick@ncdtechnologies.com, +1 608-622-7996, corresponding author)

Highlights

- Determined the effect of the three major process parameters (voltage, pulse width, and frequency) on film mechanical properties and structure
- Correlated high hardness to a few combinations of fractions of sp^3 bonding, sp^2 bonding and overall film disorder from Raman microscopy
- Applied knowledge of structure - mechanical property correlations to design multilayered thin films and establish the mechanical property limits of such multilayers
- Multilayers grown at optimal deposition conditions showed improved scratch behavior while preserving high hardness.

Abstract

Hydrogenated amorphous carbon coatings improve mechanical performance characteristics on a variety of substrates, resulting in widespread industry applications requiring a combination of high hardness, low coefficient of friction, wear resistance, elasticity, and adhesion, but such a combination of properties is difficult to achieve. We investigated the structure, mechanical properties and scratch behavior in single-layered and multilayered amorphous carbon thin films made by plasma immersion ion implantation-based plasma enhanced chemical vapor deposition. The elastic modulus and hardness in single-layered films were improved up to 149 GPa and 17 GPa respectively by varying the applied bias voltage and pulse width. We observed a non-equivalent impact on mechanical properties and coating structure based on whether pulse width or frequency were varied in the duty cycle range of 1 – 12.5%. Mechanical properties were independent of pulse frequency within experimental uncertainty. All the single-layered films showed exceptional elastic recovery of ~ 70 %. Film microstructures as measured by Raman microscopy showed that the maxima in modulus/hardness as a function of bias voltage correlated to films with the highest sp^3 bonding fraction, highest sp^2 disorder, and overall lowest disorder. The maxima in hardness and elastic modulus as a function of pulse width correlated with intermediate sp^3 bonding fraction and highest overall disorder, but the sp^2 disorder was nearly unchanged. Based on single-layer results, multilayers were developed. Nanoindentation and scratch testing showed that while multilayering preserved high hardness and improved friction behavior irrespective of the recipe, the scratch volume was strongly correlated to the hardness.

Keywords: amorphous carbon, plasma immersion ion implantation (PIII)-based Plasma Enhanced Chemical Vapor Deposition (PECVD), Raman microscopy, nanoindentation, scratch-testing

1. Introduction

Hydrogenated amorphous carbon (a-C:H) is a metastable allotrope composed of sp^2- and sp^3-hybridized carbon incorporated in an amorphous matrix. a-C:H coatings improve performance characteristics of substrates [1–8], especially hardness, wear resistance, and elastic modulus, resulting in a variety of applications with various materials requirements, such as implantable medical devices [9,10], cutting and drilling tools [11], and magnetic discs [12]. a-C:H films have been prepared by various deposition techniques such as sputtering [13,14], ion beam assisted deposition [15], cathodic arc deposition [16], plasma enhanced chemical vapor deposition [17], pulsed laser deposition [18], and plasma immersion ion implantation and deposition (PIII) [19–21]. However, functional coating surfaces require optimization of several surface properties while managing tradeoffs with other performance characteristics. For many applications, a combination of low coefficient of friction, high hardness, wear resistance, elasticity, and adhesion are highly desirable but difficult to achieve. Many beneficial properties of amorphous carbon films including high hardness and low wear rates [22] originate from sp^3 bonding, which is controlled by ion energy during deposition [23,24]. The highest sp^3 fraction is achieved with an optimal C^+ ion energy of 100 eV and is controlled by the bias voltage in conventional PECVD [25–27].

The incorporated hydrogen in a-C:H films passivates existing covalent or free bonds on the surface, greatly improving friction behavior, but mechanical properties deteriorate due to hydrogen loss from annealing and doping. Another form of amorphous carbon film with high electrical and thermal conductivities arising from large fullerene-like sp^2 clusters has been developed by combining *in situ* annealing with film growth [28,29]. However, delamination occurs due to high intrinsic compressive stress and plasma-based overheating. Alternatively, a discontinuous and periodically discharged plasma environment presents an opportunity for film

annealing while the plasma is not discharging and forming fullerene structures [30]. Starting from different precursors such as amorphous carbon and nanodiamonds and optimizing for adequate annealing conditions can form variety of fullerene structures [31], and this structural transformation is thermodynamically driven by energy minimization. This unique nanostructure comprised of hydrogen-free fullerene has interlocked and curved graphite planes and can propagate the extraordinary strength of a planar sp^2-coordinated carbon network into three dimensions. Consequently, the films have concurrently high hardnesses up to 35 GPa, friction coefficients as low as 0.05 and extremely high elasticity with an elastic recovery of 89% [32,33].

Maximizing sp^3 content was discovered to come together with high compressive film stresses (> 9 GPa) limiting the film thicknesses to ~ 100 nm before delamination occurred. Many previous studies explored techniques to reduce or eliminate intrinsic stress, revealing promise in substrate biasing during deposition [34], post deposition annealing [35] and multilayering [36,37]. Of these methods, while substrate biasing resulted in substantially lower intrinsic stress (0.5 GPa from 9 GPa), a concurrent decrease in sp^3 content drastically reduced hardness (26 GPa from 85 GPa). Post deposition annealing could eliminate the stress with unchanged film structure but required repeated cycles of deposition and annealing to make a thick adherent film. On the other hand, multilayering alternate soft and hard layers improved film adhesion onto substrates with overall low compressive stress while preserving reasonable mechanical performance [38–42]. Due to all these reasons, industry can adapt the ability to make functional multilayered films by a single process for large scale production.

Investigating deposition conditions and resultant carbon film properties continues to be an area of active interest in the scientific community [5–8], despite several previous studies that investigated such correlations. There are many reasons that support the need for current

investigation: (1) Majority of previous studies focused on selective variation of only one or two parameters. But to assess the strength and weaknesses of any deposition approach, a holistic investigation spanning available parameter space such as the one presented in current study is desired. (2) Unlike other studies employing additional plasma sources, our PIII technique offers plasma generation by the accelerating voltage itself and presents an opportunity for easy scale-up to large sample areas and processing multiple samples at the same time. Scientifically, PIII without additional plasma source deserves special attention because changing accelerating voltage and plasma properties simultaneously is a complex process. (3) Most multilayering studies focused on incorporating 'compositional' multilayers, in which the benefit comes from compositional variation across the coating thickness. Instead, this study reveals the effect of structural variation across the thickness as ion bombardment is cyclically changes to form 'structural' multilayers.

In this report, we focus on processing-structure-property correlations with an emphasis on qualitative bonding fraction and mechanical properties in hydrogenated amorphous carbon coatings. We systematically discover the structural origin of mechanical behavior in single-layered amorphous carbon thin films and then extend this understanding to develop recipes for multi-layered thin films that show a better combination of desired properties, including coefficient of friction and wear resistance, while preserving high hardness.

2. Materials and methods

2.1 Thin film deposition

Single-layered and multi-layered a-C:H thin films were deposited on single crystalline silicon substrates (mechanical grade, single side polished, thickness of 500 μm) by NCD Technologies, with a plasma immersion ion implantation-based (PIII) plasma enhance chemical vapor deposition (PECVD) set-up, as shown in Figure 1. The coating process used a periodically discharged plasma.

The process gases, Ar and methane (CH_4), were ignited to the plasma state, inducing chemical reactions and subsequent deposition at the substrate. Ar has been shown to promote dissociation degree of hydrocarbon precursors. CH_4 was chosen since it is a common precursor gas for making a-C:H by PECVD [43] and was shown to promote higher degree of crosslinking to enable a dense bonded network [44]. A DC power supply generated pulsed plasma at the substrate, with an example pulse profile shown in the inset. Film growth proceeded by energetic condensation, starting with diffusion and adsorption of the precursors onto the substrate, followed by their reaction, and finally, the reaction products were pumped away.

The plasma energy was controlled by a D.C pulser (Applied Energetics, U.S.A). A mixture of Ar + CH_4 was used as the process gas. Prior to deposition, the chamber was pumped to 2 mTorr, and the substrates were cleaned by Ar plasma for 15 minutes at pressure of 30 mTorr, D.C. pulse of 5.0 kV, 5kHz, and 10 μs. The deposition pressure was 150 mTorr. For every deposition, 4 pieces of Si squares (10 mm X 10 mm) were equally spaced on the copper sample stage of Φ65mm to which the D.C. pulse was applied.

Single-layered thin films were deposited to systematically study the effect of three control parameters: applied D.C. voltage, pulse width and frequency. All the parameters are listed in Table 1. The deposition voltage was varied from 1.02 kV to 6.11 kV at a pulse width of 5.5 μs and frequency of 5.0 kHz. The pulse width was varied from 2.0 μs to 25.0 μs (duty cycle of 1 to 12.5 %) at a voltage of 2.5 kV and frequency of 5.0 kHz. The frequency was varied from 1.0 kHz to 16.0 kHz (duty cycle of 0.6 to 8.8 %), at pulse width of 5.5 μs and voltage of 2.5 kV.

Two sets of 800 nm thick multilayered recipes (total of seven samples) were prepared: (1) three samples with alternating 10 nm thick layers grown at 1.02 kV and 10, 20 and 30 nm grown at 1.94 kV, one sample with alternating 20 nm, layers, each grown at 1.02 kV and 1.94 kV, and (2) three

samples with alternating 10 nm layers grown at 6.11 kV and 10, 20 and 30 nm grown at 1.94 kV. For all the multilayered samples, the pulse width and frequency were set at 5.5 μs and 5.0 kHz respectively.

2.2 Preliminary characterization

The deposition rate for single-layer coatings was calculated by dividing the film thicknesses measured with Single-Spot Thickness Measurement F20 (Filmetrics, U.S.A.) by the deposition time. All the films had thicknesses of 800-1243 nm. The thickness of the individual multilayers was estimated based on the knowledge of deposition rates for single layers. The film structure was characterized by a Thermo-Fisher Scientific (U.S.A.) DXRxi Raman Imaging microscope with 532 nm Ar laser as excitation source, laser energy of 10 mW, exposure time of 0.2 seconds per scan and 50 scans per spectrum. The Raman spectra were first background-subtracted with a spline fit and then fitted based on two Gaussian curve shapes (one for G peak and another for D peak, explained further in results section) in Origin software. The ratio of intensities from D and G peaks, I(D)/I(G) was calculated based on areas under the curve.

2.3 Mechanical properties

The single-layered and multi-layered films' hardness (H) and reduced elastic modulus (E_r) were investigated by nanoindentation experiments, using a Hysitron (U.S.A.) TI950 Triboindenter with a Berkovich diamond tip. Prior to running these experiments, the instrument was verified to be satisfactorily calibrated by indenting a standard fused silica sample. Triboscan software provided by the instrument maker digitally recorded the load-displacement characteristics while indenting and the H and E_r values were calculated by fitting the unloading curves to a power law,

as per the Oliver-Pharr method [45]. Prior to analysis, all curves were properly zeroed using Triboscan software. H values reported in this study are as per the Meyer formula [46]

$$H = \frac{F}{A_c} \quad (1)$$

E_r values are determined by

$$E_r = \frac{0.5 \times (dF/dh)}{\sqrt{(A_c/\pi)}} \quad (2)$$

where F, A_c and h are the applied force, contact area and depth, respectively. The elastic modulus (E) was calculated from

$$\frac{1}{E_r} = \frac{(1-\upsilon^2)}{E} + \frac{(1-\upsilon_i^2)}{E_i} \quad (3)$$

where υ and υ_i are Poisson ratios for carbon coatings and the diamond indenter respectively, and E_i is the elastic modulus of the diamond indenter (υ = 0.22 [47], E_i = 1141 GPa, υ_i = 0.07 [48]). The residual (h_{res}) to maximum depth (h) ratio showed that pile-up effect is negligible in our measurements since $h_{res}/h < 0.7$ [48]. To minimize the substrate effect, all the indentations were limited to less than 15% of the total film thickness. All data points were averages of at least 10 indentations using the same condition of a trapezoidal loading function with peak load of 2 mN.

2.4 Scratch testing

Coefficient of friction measurements by scratch testing with diamond tip were performed on the films by using the nanoscratch feature of Hysitron (U.S.A.) TI950 Triboindenter. In this instrument setting, a normal load is applied by a horizontal capacitive transducer while the lateral force experienced by the scratching tip is measured by two vertical capacitive transducers with load and normal displacement resolutions of 3 μN and 0.04 nm respectively. Using a spherical tip

of diameter 1 μm, scratches of length 10 μm were made at constant loads of 3, 6 and 10 mN. The loading cycle was performed with the following steps: first, the tip moved 5 μm to one side of the mean position; then, load was applied over 5 seconds during which the instrument recorded sample surface profile to be later used for tilt correction; finally, after reaching peak load, the tip started scratching at a speed of 0.57 μm/s and the load was withdrawn over 5 seconds after a scratch distance of 10 μm. Post-scratching, the same tip was used for imaging at a contact load of 3 μN and the resulting scanning probe microscopy (SPM) images were analyzed by Triboscan and Gwyddion [49] software packages to extract scratch profiles.

3. Results and discussion

3.1 Dependence of deposition rate on growth parameters

Figure 2 summarizes monotonically increasing deposition rate as a function of increasing bias voltage, pulse width and frequency. By employing a PIII-based PECVD for a-C:H thin film fabrication, a D.C. pulser served as an ionization power source and hydrocarbon precursors were used as the carbon source. The pulser supplied variable bias voltage to easily tune the ionization and the C^+ ions' energies in the deposition process and consequently, the sp^3 content of the films. Also, the variable substrate bias voltage and duty cycle (varied by changing pulse width and frequency) enable the annealing temperature and time to be optimized during the discharging period to control the sp^2 fullerene-like carbon fraction, resulting in the ability to span the structural spectrum of hard a-C:H with high sp^3 and soft-tensile a-C:H with high abundances of fullerene structures.

3.2 Structural characterization of single-layered thin films

Raman spectroscopy has been reported to reveal subtle microstructural changes in carbon films. Typical Raman spectra on a-C:H films are characterized by a G (graphitic) band around 1550 cm^{-1} and a D (disorder-induced) band around 1380 cm^{-1}, originating in the size, distribution and breathing modes of sp^2 sites [50–52]. While the Raman scattering from sp^2 sites is 50 times stronger than sp^3 [53], qualitative trends in sp^3/sp^2 can still be inferred [54,55]. Figure 3 shows fitting an example background-subtracted Raman spectrum to D and G peaks for one of the thin film samples. We observe good fits for all Raman spectra (R-squared values ~ 0.999) using the conventional method of fitting only for D and G bands.

Figure 4 shows Raman spectroscopy measurements on single-layered films as a function of the deposition voltage. The I(D)/I(G) value first decreases from 0.87 to 0.52 as the voltage is increased from 1.01 kV to 1.94 kV. At voltages above 1.94 kV, the I(D)/I(G) ratio monotonically increases up to 1.28. The G-peak position stays at 1530-1531 cm^{-1} for voltage values from 1.01 to 1.94 kV and then increases slightly up to 1544 cm^{-1}. Taken together, the trends in I(D)/I(G) ratios [56] and G-peak [57] values suggest that maximizing sp^3 contribution to the film structure requires an optimal voltage. The D-peak position first decreases from 1361 cm^{-1} to 1345 cm^{-1} as the voltage increases from 1.01 to 1.94 kV, becomes constant at 1373 - 1375 cm^{-1} for voltages from 2.50 to 5.00 kV and rises slightly to 1382 cm^{-1} at a voltage of 6.11 kV. This reveals that the overall structural disorder, smaller aromatic rings and ordered aromatic rings first decrease for voltages of 1.01 – 1.94 kV and then increase from 2.50 – 6.11 kV [50]. The G full-width at half maximum (FWHM) increases from 144 to 153 cm^{-1} as voltage is increased from 1.01 to 1.94 kV and then decreases monotonically to 137 cm^{-1} at 6.11 kV. The trends in G FWHM suggest sp^2 disorder is maximum at voltage of 1.94 kV [57]. For voltages above 1.94 kV, we suggest that the ion

bombardment from increasing bias voltage is strong enough to raise the substrate temperature and contribute to graphitization of film structure meaning some sp^3 fraction gets converted to sp^2.

Duty cycle or the plasma on-off time ratio was varied by independently changing pulse width and frequency, akin to increasing the annealing time at constant bias voltage (or annealing temperature). Figure 5 shows Raman spectroscopy measurements on single-layered films as a function of the pulse width. I(D)/I(G) increases from 0.68 to 1.00 as the pulse width is increased from 2 to 25 μs. The G-peak position increases slightly from 1529 cm^{-1} up to 1536 cm^{-1}. Taken together, the trends in I(D)/I(G) ratios and G-peak values suggest that sp^3 contribution to the film structure increases as pulse width is increased. The D-peak position peaks to 1372 cm^{-1} at a pulse width of 5.5 μs and stays nearly the same for pulse width values from 9 to 25 μs. These data show that the contribution of overall structural disorder, smaller aromatic rings and ordered aromatic rings to the film structure is maximum at 5.5 μs. The G FWHM decreases somewhat with increasing pulse width, suggesting sp^2 disorder also decreases.

Figure 6 shows Raman spectroscopy measurements on single-layered films as a function of the frequency. I(D)/I(G) increases from 0.68 to 0.95 as the frequency is increased from 2.5 to 10 kHz and decreases to 0.77 with further increase up to 16 kHz. The G-peak position increases slightly from 1532 cm^{-1} up to 1535 cm^{-1}. Taken together, the trends in I(D)/I(G) ratios and G-peak values suggest that sp^3 contribution to the film structure peaks at an optimal frequency value. The D-peak position first decreases from 1372 cm^{-1} to 1362 cm^{-1} as the frequency increases from 2.5 to 10 kHz and rises back up to 1371 cm^{-1} at a frequency of 16 kHz. These data show that the overall structural disorder, smaller aromatic rings and ordered aromatic rings first decrease for frequencies of 2.5 – 10 kHz and then increases from 12.5 to 16 kHz. The G-FWHM is consistently between 147 – 149 cm^{-1} suggesting sp^2 disorder is nearly the same irrespective of frequencies.

By itself, Raman microscopy likely is not able to differentiate between graphitic- and fullerene-like structures. Previous literature studies have relied on a combination of advanced structural characterization techniques [58,59] and simulations [31] to identify presence of fullerene-like structures as a function of duty cycle. Ji et al. [58] directly observed ordered fullerene-like domains of several nanometers in size at a duty cycle of 20 %. These domains decreased in size as the duty cycle was increased up to 100%. Wang et al. [59] reported formation of C_{60} and fullerene nanoparticles at duty cycle of 60 %. In comparison, the current study has explored relatively low duty cycles between 1 and 12.5 %. Lau et al. [31] found that fullerene-like carbon structures are thermodynamically driven and can be formed from a variety of precursors including amorphous and sp^3-bonded carbon. They also identified that a conducive background gas pressure was critical to form fullerene-like structures. A discontinuous and periodically discharged plasma has been shown to promote fullerene-like structures [58,59]. But actual realization of such structures is heavily influenced by process parameters, requiring an in-depth understanding of the nucleation mechanisms and the complete range of possible microstructures. At face value, the current Raman spectroscopy results could not clearly identify emergence of fullerene-like structures as the duty cycle was lowered and should be pursued further using advanced structural characterization techniques. Nevertheless, our Raman results still present valuable insights into subtle changes in coating microstructure.

Carbon bonding and hydrogen content are interconnected, making it difficult to study them independently. Hydrogen in a-C:H modifies its C-C network, with high H content saturating C=C bonds as $C{\equiv}CH_x$ rather than increasing the fraction of C-C bonds [50,51]. sp^2 bonding dominates at low H content while sp^3 bonding is prevalent at intermediate H content [50]. Our results are consistent with other studies in literature relating overall reduction in the films' bonded hydrogen

content as the annealing temperature is increased [30] since increasing the bias voltage is analogous to increasing the films' annealing temperature [60]. In a previous study, H content in a-C:H went down from 50 to < 30 % as bias voltage was increased from 200 to 1000 V using CH_4 as precursor [53]. Further, Wang et al. found that using a pulsed D.C. plasma source, low H promoted fullerene-like arrangement, inhibited amorphous carbon formation and induced curvature/cross-linking of graphitic layers [32]. Since all our bias voltages are above 1000 V, we expect bonding nature and fractions to dominate over hydrogen content thus contributing significantly to the film structure and mechanical properties, further supported by a small peak at ~850-860 cm^{-1} in Raman spectra for all coatings (seen in figure 3).

3.3 Mechanical properties of single- and multi-layered films

Figure 7 summarizes mechanical properties of single-layered thin films as a function of the deposition voltage, pulse width and frequency. The elastic recovery %, R is defined as $((h_{max} - h_{res}) \times 100)/h_{max}$, where h_{max} and h_{res} are the maximum indentation depth and residual depth [61]. R for all these films is 65 – 70 %. Figure 7 (a) shows H and E increase initially as bias voltage is increased, showing a peak in H and E at a voltage of 2.5 kV, and then become softer as the bias voltage is increased above 2.5 kV. The peak in mechanical properties coincides with the highest sp^3 fraction, highest sp^2 disorder and overall lowest disorder from the Raman data in Figure 4. The trends in H and E with varying bias voltage are supported by the Raman data and are consistent with previous studies. In comparison, An et al. observed peak in H and E at 1.5 – 3.5 kV and duty cycle of 0.5%, which compares reasonably well to our observations. Sheeja et al. have shown that maximizing sp^3 bonding requires an optimal carbon ion energy as controlled by bias voltage and promotes high hardness [34]. This optimal energy results from a balance between carbon ions having sufficient energy to penetrate the thin surface layer and not having excess energy that would

dissipate and heat up the coating. Above this critical bias voltage, excess energy from deposition can convert sp^3 bonding to graphite-like sp^2 bonding, causing deterioration of mechanical properties.

We varied the duty cycle in about the same range (1 – 12.5%) by independently changing pulse width and pulse frequency. Figure 7(b) shows H and E values increased initially as the pulse width was increased, peaked at a pulse width of 9 μs, and then went down except the last point at 25 μs. This peak in mechanical properties correlated to intermediate sp^3 contribution and highest overall disorder from the Raman data from Figure 5. Figure 7 (c) shows that varying the frequency does not alter the mechanical properties significantly, but there is a peak in H and E at a frequency of 2.5 kHz, which corresponds to the highest sp^3 order, lowest sp^2 disorder and highest overall disorder as seen from Figure 6. Several studies have explored the impact of varying duty cycle between 20 - 100% and observed a monotonic increase in mechanical properties as duty cycle was decreased, originating in fullerene-like structures [32,58,62]. Whether lowering the duty cycle further below 20% has any benefit remains an open question. Limited number of studies exist exploring impact of duty cycle below 20% [20] and deserve to be explored to optimize formation conditions of fullerene-like structures and their impact on mechanical properties. Towards that end, our observations indicate a non-equivalent impact on mechanical properties and coating structure based on whether pulse width or frequency were varied in the duty cycle range of 1 – 12.5%.

H/E ratio represents resistance of a material relative to elastic deformation, while H^3/E^2 represents its resistance to plastic deformation [63,64]. Qualitatively, higher values of these ratios predict higher wear resistance [65]. H/E for a-C:H coatings is typically ~ 0.1, with lower values suggesting elastoplastic behavior and higher values indicating elastic behavior. Figure 8(a) shows

that resistance to elastic deformation is relatively high (as per H/E values) for films grown at voltages up to 2.5 kV. At higher voltage, H/E decreases, except for the film grown at 6.11 kV. The resistance to plastic deformation (as per H^3/E^2 values) shows a clear peak at 2.5 kV and then decreases with increasing voltage (except at 6.11 kV). Figure 8(b) shows a peak in resistance to elastic and plastic deformation at a pulse width of 17 μs, but this peak does not correspond to the highest measured mechanical properties in Figure 7(b). Figure 8(c) does not show a clear trend in resistances to elastic and plastic deformations due to frequency.

Next, we investigated mechanical and scratch behavior of multilayered coatings with alternating hard-soft layers. Based on structure-mechanical property characterization of single-layered coatings as noted above, we identified that voltage and pulse width seem to have a profound effect on film microstructure, while frequency is a less important parameter. Optimizing the various control parameters could span the accessible elastic modulus and hardness values in single-layered films up to 149 GPa and 17 GPa respectively. We chose to control the hard-soft layers with bias voltage. Figure 9 compares mechanical properties of multilayered thin films to those of constituent single-layered films. Figure 9 (a) shows that multilayering can vary the film hardness from + 2.0 % to – 9.3 %, meaning high hardness can be preserved. Consistent with our observations, published studies have shown that hardness values for multilayers are expected to be between the hard and soft single-layer limits [36,41,66], but it is also possible to exceed the hardness of hardest layer with optimal coating architecture utilizing well-tuned deposition conditions and bilayer thickness [37]. Figure 9 (b) shows that elastic modulus is much more sensitive to multilayering (between + 0.7 % and – 24.3 %). Since elastic modulus is a proxy for film density, these results suggest that multilayering may introduce less dense regions at the interfaces. Figure 9 (c) and (d) shows that multilayering improves both H/E and H^3/E^2 values as

much as + 27.3 % and + 57.5 % as compared to the corresponding best performing single-layered films, indicating promise for better wear resistance due to multilayering as compared to single layers [65,67].

3.4 Scratching – coefficient of friction & wear

Figure 10 shows coefficient of friction (CoF) behavior for single-layered and multi-layered films as the diamond tip was scratched across samples for 10 μm at 6 and 10 mN. Data for 3 mN scratches was noisy, possibly due to surface roughness effects, but the CoF data at 6 and 10 mN were very repeatable. For the single-layered films, the hard and intermediate samples had a lower CoF than the soft sample. Multilayering clearly reduced the CoF irrespective of the recipe used. For the hard-soft system, alternating 20 nm layers of hard-soft layers showed the best friction resistance. For the hard-intermediate system, alternating 10 nm layers of hard and intermediate layers showed best friction resistance.

Figure 11 shows the SPM images of scratches made on the single-layered films at peak load of 10 mN. The hard film shows the lowest scratch depth amongst the single-layered films and can be directly correlated to the CoF and hardness behaviors. Figure 12 shows SPM images of scratches made on hard-soft multilayered film system at peak load of 10 mN. Only the film grown with alternating 20 nm interlayers shows a better scratch resistance than the hard film, while other films show scratch resistance worse than the single-layered hard film. This multilayered film also has the lowest CoF and highest hardness of all. Figure 13 shows SPM images of scratches made on hard-intermediate multilayer system at peak load of 10 mN. All of these films show worse scratch resistance, better CoF, and lower hardness than the hard film. The scratch depths reported here are true values measured upon recovery after the actual scratch tests. Our results indicate that while the CoF can be consistently lowered by multilayering, the scratch resistance (and hence the

wear resistance) seems to be dictated by the material's response to mechanical deformation (or in other words, hardness).

Nanomechanical measurements from this study showed that it is possible to develop multilayer coating recipes with high hardness and improved scratch and friction behavior as compared to single layers. Particularly, we showed that a hard/soft architecture together with an optimal bilayer thickness of 20 nm each preserved the hardness as high as hardest single layer, showed the lowest CoF < 0.1 and H/E as well as H^3/E^2 values higher than any single-layered coating. This is broadly consistent with previous studies that showed deposition of alternating soft layer rich in sp^2 carbon and hard layer rich in sp^3 carbon enable stress relaxation, improved adherence to substrate and protects against crack initiation [66,68,69]. Based on numerous previous studies, the interfacial regions in multilayers are thought to deflect crack energy by accommodating bulk of the plastic deformation, thus contributing to improved friction behavior, wear resistance and adhesion [42]. A low bilayer thickness of 14 – 20 nm achieved the best combination of hardness, modulus, residual stress, CoF and wear resistance in a-C:H/Si-doped a-C:H multilayers [40]. Similarly, bilayer periodicity of 5 – 10 nm in sputtered WC/DLC multilayers showed a minima in residual stress, and improved wear resistance and adhesion while hardness maxima occurred at 20 nm [39]. Our optimal bilayer thickness of 20 nm together with hard and soft multilayering shows a qualitatively similar result.

Clearly, individual layer structure/properties as well as bilayer periodicity have a strong influence on multilayer performance and these correlations need to be resolved from an engineering design perspective. This study shows the need for further mechanistic investigation since scratching is a dynamic process with interplay between abrasive, adhesive and shearing mechanisms and is influenced strongly by hydrogen content in addition to coatings' stress state.

Presence of hydrogen is inherent to improved friction behavior since low friction coefficient is thought to be related to hydrogen release and graphitization [70]. Additionally, comparing friction coefficient values requires caution, since they are very sensitive to the testing conditions. Going forward, PIII-based PECVD method has potential to tune structures in amorphous carbon coatings and promises to expand the multilayered protective coatings available beyond state of the art.

In summary, this study demonstrates the controllability of coating properties using PIII-based PECVD approach, both by optimizing for process parameters in single-layer recipes and by multilayering. Our fabrication method presents a powerful deposition technique that can access a wide range of carbon structures and resulting mechanical, wear, and scratch properties. Our results are particularly relevant since amorphous carbon coatings are currently being deployed in a variety of real-world applications. Further, the present fabrication technique can be expanded to develop doped and composite carbon coatings [18,21]. Therefore, industry will benefit from PIII-based PECVD manufacturing routes, tailoring coating recipes to match end user product specifications.

4. Conclusions

We investigated the structure, mechanical properties and scratch behavior in single-layered and multilayered amorphous carbon thin films made by plasma immersion ion implantation-based plasma enhanced chemical vapor deposition. Varying the applied bias voltage and pulse width can improve the elastic modulus and hardness in single-layered films up to 149 GPa and 17 GPa respectively. We observed a non-equivalent impact on mechanical properties and coating structure based on whether pulse width or frequency were varied in the duty cycle range of 1 – 12.5%. Mechanical properties were independent of pulse frequency within experimental uncertainty. Raman microscopy on single-layered films showed that the maximum mechanical properties as a function of bias voltage coincided with highest sp^3 fraction, highest sp^2 disorder and overall lowest

disorder. The maximum mechanical properties as a function of pulse width coincided with intermediate sp^3 contribution and highest overall disorder, while the sp^2 disorder remained nearly constant. Nanoindentation and scratch-testing showed that the scratch volume was strongly correlated to the hardness and multilayering preserved high hardness and improved friction behavior irrespective of the recipe. Particularly, we showed that a hard/soft architecture together with an optimal bilayer thickness of 20 nm each preserved the hardness as high as hardest single layer, showed the lowest CoF < 0.1 and H/E as well as H^3/E^2 values higher than any single-layered coating.

Acknowledgments

This work was supported by the Advanced Materials Industrial Consortium (AMIC) of the Wisconsin Materials Research Science and Engineering Center (MRSEC, NSF DMR-1720415). Thickness measurements by Dr. Mike Efremov and access to characterization facilities supported by the Wisconsin MRSEC are also deeply appreciated.

Data Availability Statement

The raw data used in this study is available from the authors upon reasonable request.

References

[1] J. Robertson, Properties of diamond-like carbon, Surf. Coatings Technol. 50 (1992) 185–203. doi:10.1016/0257-8972(92)90001-Q.

[2] J. Robertson, Diamond-like amorphous carbon, Mater. Sci. Eng. R Reports. 37 (2002) 129–281. doi:10.1016/S0927-796X(02)00005-0.

[3] J.C. Angus, C.C. Hayman, Low-Pressure , Metastable Growth of Diamond and "Diamondlike" Phases, Science (80-.). 241 (1988) 913–921. https://www.jstor.org/stable/1702445.

[4] A.A. Voevodin, M.S. Donley, Preparation of amorphous diamond-like carbon by pulsed laser deposition: A critical review, Surf. Coatings Technol. 82 (1996) 199–213. doi:10.1016/0257-8972(95)02734-3.

[5] W. Koszela, P. Pawlus, R. Reizer, T. Liskiewicz, The combined effect of surface texturing and DLC coating on the functional properties of internal combustion engines, Tribol. Int. 127 (2018) 470–477. doi:10.1016/j.triboint.2018.06.034.

[6] M. Jokari-Sheshdeh, F. Mahboubi, K. Dehghani, Structure and tribological behavior of diamond-like carbon coatings deposited on the martensitic stainless steel: The influence of gas composition and temperature, Diam. Relat. Mater. 81 (2018) 77–88. doi:10.1016/j.diamond.2017.11.007.

[7] R.G. Toro, P. Calandra, B. Cortese, T. de Caro, M. Brucale, A. Mezzi, F. Federici, D. Caschera, Argon and hydrogen plasma influence on the protective properties of diamond-like carbon films as barrier coating, Surfaces and Interfaces. 6 (2017) 60–71.

doi:10.1016/j.surfin.2016.11.009.

[8] F. Faraldi, E. Angelini, C. Riccucci, A. Mezzi, D. Caschera, S. Grassini, Innovative diamond-like carbon coatings for the conservation of bronzes, Surf. Interface Anal. 46 (2014) 764–770. doi:10.1002/sia.5367.

[9] R. Hauert, K. Thorwarth, G. Thorwarth, An overview on diamond-like carbon coatings in medical applications, Surf. Coatings Technol. 233 (2013) 119–130. doi:10.1016/j.surfcoat.2013.04.015.

[10] A. Grill, Diamond-like carbon coatings as biocompatible materials - An overview, Diam. Relat. Mater. 12 (2003) 166–170. doi:10.1016/S0925-9635(03)00018-9.

[11] P.J. Heaney, A. V. Sumant, C.D. Torres, R.W. Carpick, F.E. Pfefferkorn, Diamond coatings for micro end mills: Enabling the dry machining of aluminum at the micro-scale, Diam. Relat. Mater. 17 (2008) 223–233. doi:10.1016/j.diamond.2007.12.009.

[12] P.R. Goglia, J. Berkowitz, J. Hoehn, A. Xidis, L. Stover, Diamond-like carbon applications in high density hard disc recording heads, Diam. Relat. Mater. 10 (2001) 271–277. doi:10.1016/S0925-9635(00)00589-6.

[13] N. Savvides, Optical constants and associated functions of metastable diamondlike amorphous carbon films in the energy range 0.5-7.3 eV, J. Appl. Phys. 59 (1986) 4133–4145. doi:10.1063/1.336672.

[14] K. Bewilogua, R. Wittorf, H. Thomsen, M. Weber, DLC based coatings prepared by reactive d.c. magnetron sputtering, Thin Solid Films. 447–448 (2004) 142–147. doi:10.1016/S0040-6090(03)01088-5.

[15] E.G. Spencer, P.H. Schmidt, D.C. Joy, F.J. Sansalone, Ion-beam-deposited polycrystalline diamondlike films, Appl. Phys. Lett. 29 (1976) 118–120. doi:10.1063/1.88963.

[16] A. Anders, N. Pasaja, S.H.N. Lim, T.C. Petersen, V.J. Keast, Plasma biasing to control the growth conditions of diamond-like carbon, Surf. Coatings Technol. 201 (2007) 4628–4632. doi:10.1016/j.surfcoat.2006.09.313.

[17] A. Pauschitz, J. Schalko, T. Koch, Nanoindentation and AFM studies of PECVD DLC and reactively sputtered Ti containing carbon films, Bull. Mater. Sci. 26 (2003) 585–591.

[18] Q. Wei, A.K. Sharma, J. Sankar, J. Narayan, Mechanical properties of diamond-like carbon composite thin films prepared by pulsed laser deposition, Compos. Part B. 30 (1999) 675–684.

[19] G. Thorwarth, C. Hammerl, M. Kuhn, W. Assmann, B. Schey, B. Stritzker, Investigation of DLC synthesized by plasma immersion ion implantation and deposition, Surf. Coatings Technol. 193 (2005) 206–212. doi:10.1016/j.surfcoat.2004.07.061.

[20] X. An, Z. Wu, L. Liu, T. Shao, S. Xiao, S. Cui, H. Lin, R.K. Fu, X. Tian, P.K. Chu, F. Pan, High-ion-energy and low-temperature deposition of diamond-like carbon (DLC) coatings with pulsed kV bias, Surf. Coatings Technol. 365 (2019) 152–157. doi:10.1016/j.surfcoat.2018.08.099.

[21] L. Liu, Z. Wu, X. An, S. Xiao, S. Cui, H. Lin, R.K.Y. Fu, X. Tian, R. Wei, P.K. Chu, F. Pan, Excellent adhered thick diamond-like carbon coatings by optimizing hetero-interfaces with sequential highly energetic Cr and C ion treatment, J. Alloys Compd. 735 (2018) 155–162. doi:10.1016/j.jallcom.2017.11.057.

[22] A. Gangopadhyay, Mechanical and tribological properties of amorphous carbon films, Tribol. Lett. 5 (1998) 25–39. doi:10.1023/A:1019152515982.

[23] W. Jacob, W. Möller, On the structure of thin hydrocarbon films, Appl. Phys. Lett. 63 (1993) 1771–1773. doi:10.1063/1.110683.

[24] P. Reinke, W. Jacob, W. Möller, Influence of the ion energy on the growth and structure of thin hydrocarbon films, J. Appl. Phys. 74 (1993) 1354–1361. doi:10.1063/1.354892.

[25] M. Weiler, S. Sattel, K. Jung, H. Ehrhardt, V.S. Veerasamy, J. Robertson, Highly tetrahedral, diamond-like amorphous hydrogenated carbon prepared from a plasma beam source, Appl. Phys. Lett. 64 (1994) 2797–2799. doi:10.1063/1.111428.

[26] C. Wild, P. Koidl, Structured ion energy distribution in radio frequency glow-discharge systems, Appl. Phys. Lett. 54 (1989) 505–507. doi:10.1063/1.100913.

[27] C. Wild, P. Koidl, Ion and electron dynamics in the sheath of radio-frequency glow discharges, J. Appl. Phys. 69 (1991) 2909–2922. doi:10.1063/1.348601.

[28] N. Xu, H.T.E. Teo, M. Shakerzadeh, X. Wang, C.M. Ng, B.K. Tay, Electrical properties of textured carbon film formed by pulsed laser annealing, Diam. Relat. Mater. 23 (2012) 135–139. doi:10.1016/j.diamond.2012.01.016.

[29] C.W. Tan, S. Maziar, E.H.T. Teo, B.K. Tay, Microstructure and through-film electrical characteristics of vertically aligned amorphous carbon films, Diam. Relat. Mater. 20 (2011) 290–293. doi:10.1016/j.diamond.2011.01.010.

[30] H. Li, T. Xu, C. Wang, J. Chen, H. Zhou, H. Liu, Annealing effect on the structure, mechanical and tribological properties of hydrogenated diamond-like carbon films, Thin

Solid Films. 515 (2006) 2153–2160. doi:10.1016/j.tsf.2006.04.018.

[31] D.W.M. Lau, D.G. McCulloch, N.A. Marks, N.R. Madsen, A. V. Rode, High-temperature formation of concentric fullerene-like structures within foam-like carbon: Experiment and molecular dynamics simulation, Phys. Rev. B - Condens. Matter Mater. Phys. 75 (2007) 3–6. doi:10.1103/PhysRevB.75.233408.

[32] Y. Wang, K. Gao, Q. Wang, J. Zhang, The correlation between nano-hardness and elasticity and fullerene-like clusters in hydrogenated amorphous carbon films, Chem. Phys. Lett. 692 (2018) 258–263. doi:10.1016/j.cplett.2017.12.032.

[33] Z. Wang, Z. Gong, B. Zhang, Y. Wang, K. Gao, J. Zhang, G. Liu, Heating induced nanostructure and superlubricity evolution of fullerene-like hydrogenated carbon films, Solid State Sci. 90 (2019) 29–33. doi:10.1016/j.solidstatesciences.2019.01.011.

[34] D. Sheeja, B.K. Tay, S.P. Lau, X. Shi, Tribological properties and adhesive strength of DLC coatings prepared under different substrate bias voltages, Wear. 249 (2001) 433–439. doi:10.1016/S0043-1648(01)00541-5.

[35] P. Zhang, B.K. Tay, C.Q. Sun, S.P. Lau, Microstructure and mechanical properties of nanocomposite amorphous carbon films, J. Vac. Sci. Technol. A Vacuum, Surfaces, Film. 20 (2002) 1390–1394. doi:10.1116/1.1486227.

[36] S. Anders, D.L. Callahan, G.M. Pharr, T.Y. Tsui, C.S. Bhatia, Multilayers of amorphous carbon prepared by cathodic arc deposition, Surf. Coatings Technol. 94–95 (1997) 189–194. doi:10.1016/S0257-8972(97)00346-0.

[37] S. Logothetidis, S. Kassavetis, C. Charitidis, Y. Panayiotatos, A. Laskarakis,

Nanoindentation studies of multilayer amorphous carbon films, Carbon N. Y. 42 (2004) 1133–1136. doi:10.1016/j.carbon.2003.12.054.

[38] F. Li, S. Zhang, J. Kong, Y. Zhang, W. Zhang, Multilayer DLC coatings via alternating bias during magnetron sputtering, Thin Solid Films. 519 (2011) 4910–4916. doi:10.1016/j.tsf.2011.01.052.

[39] B.R. Pujada, F.D. Tichelaar, G.C.A.M. Janssen, Hardness of and stress in tungsten carbide–diamond like carbon multilayer coatings, Surf. Coatings Technol. 203 (2008) 562–565. doi:10.1016/j.surfcoat.2008.05.051.

[40] C. Chouquet, C. Ducros, S. Barrat, A. Billard, F. Sanchette, Mechanical properties of a-C:H/Si-containing a-C:H multilayered coatings grown by LF-PECVD, Surf. Coatings Technol. 203 (2008) 745–749. doi:10.1016/j.surfcoat.2008.08.008.

[41] Y. Lin, A.W. Zia, Z. Zhou, P.W. Shum, K.Y. Li, Development of diamond-like carbon (DLC) coatings with alternate soft and hard multilayer architecture for enhancing wear performance at high contact stress, Surf. Coatings Technol. 320 (2017) 7–12. doi:10.1016/j.surfcoat.2017.03.007.

[42] T. Weikert, S. Wartzack, M.V. Baloglu, K. Willner, S. Gabel, B. Merle, F. Pineda, M. Walczak, M. Marian, A. Rosenkranz, S. Tremmel, Evaluation of the surface fatigue behavior of amorphous carbon coatings through cyclic nanoindentation, Surf. Coatings Technol. 407 (2021) 126769. doi:10.1016/j.surfcoat.2020.126769.

[43] W. Zhang, Y. Catherine, Deposition of carbon films by the dissociation of methane in r.f. discharge, Surf. Coatings Technol. 47 (1991) 69–83. doi:10.1016/0257-8972(91)90269-3.

[44] D. Thiry, A. De Vreese, F. Renaux, J.L. Colaux, S. Lucas, Y. Guinet, L. Paccou, E. Bousser, R. Snyders, Toward a Better Understanding of the Influence of the Hydrocarbon Precursor on the Mechanical Properties of a-C:H Coatings Synthesized by a Hybrid PECVD/PVD Method, Plasma Process. Polym. 13 (2016) 316–323. doi:10.1002/ppap.201500050.

[45] W.C. Oliver, G.M. Pharr, An improved technique for determining hardness and elastic modulus using load and displacement sensing indentation experiments, J. Mater. Res. 7 (1992) 1564–1583. doi:10.1557/JMR.1992.1564.

[46] M. Sakai, Meyer hardness: A measure for plasticity?, J. Mater. Res. 14 (1999) 3630–3639. doi:10.1557/JMR.1999.0490.

[47] X. Jiang, K. Reichelt, B. Stritzker, Mechanical properties of a -C:H films prepared by plasma decomposition of C 2 H 2, J. Appl. Phys. 68 (1990) 1018–1022. doi:10.1063/1.346738.

[48] G.M. Pharr, Measurement of mechanical properties by ultra-low load indentation, Mater. Sci. Eng. A. 253 (1998) 151–159. doi:10.1016/s0921-5093(98)00724-2.

[49] D. Nečas, P. Klapetek, Gwyddion: an open-source software for SPM data analysis, Open Phys. 10 (2012) 181–188. doi:10.2478/s11534-011-0096-2.

[50] A.C. Ferrari, J. Robertson, Interpretation of Raman spectra of disordered and amorphous carbon, Phys. Rev. B. 61 (2000) 14095–14107. doi:10.1103/PhysRevB.61.14095.

[51] C. Casiraghi, A.C. Ferrari, J. Robertson, Raman spectroscopy of hydrogenated amorphous carbons, Phys. Rev. B. 72 (2005) 085401. doi:10.1103/PhysRevB.72.085401.

[52] J. Schwan, S. Ulrich, V. Batori, H. Ehrhardt, S.R.P. Silva, Raman spectroscopy on amorphous carbon films, J. Appl. Phys. 80 (1996) 440–447. doi:10.1063/1.362745.

[53] M.A. Tamor, W.C. Vassell, Raman "fingerprinting" of amorphous carbon films, J. Appl. Phys. 76 (1994) 3823–3830. doi:10.1063/1.357385.

[54] G. Irmer, A. Dorner-Reisel, Micro-Raman studies on DLC coatings, Adv. Eng. Mater. 7 (2005) 694–705. doi:10.1002/adem.200500006.

[55] A. Merlen, J. Buijnsters, C. Pardanaud, A Guide to and Review of the Use of Multiwavelength Raman Spectroscopy for Characterizing Defective Aromatic Carbon Solids: from Graphene to Amorphous Carbons, Coatings. 7 (2017) 153. doi:10.3390/coatings7100153.

[56] Y.R. Jeng, P.C. Tsai, K. Te Wu, Y.M. Wang, F.C.N. Hong, S.M. Huang, K.C. Chen, Effect of feed gas composition effects on the nanotribological properties of diamond-like carbon films, Thin Solid Films. 529 (2013) 301–305. doi:10.1016/j.tsf.2012.03.107.

[57] A. Modabberasl, P. Kameli, M. Ranjbar, H. Salamati, R. Ashiri, Fabrication of DLC thin films with improved diamond-like carbon character by the application of external magnetic field, Carbon N. Y. 94 (2015) 485–493. doi:10.1016/j.carbon.2015.06.081.

[58] L. Ji, H. Li, F. Zhao, W. Quan, J. Chen, H. Zhou, Effects of pulse bias duty cycle on fullerenelike nanostructure and mechanical properties of hydrogenated carbon films prepared by plasma enhanced chemical vapor deposition method, J. Appl. Phys. 105 (2009) 106113. doi:10.1063/1.3125528.

[59] Q. Wang, C. Wang, Z. Wang, J. Zhang, D. He, Fullerene nanostructure-induced excellent

mechanical properties in hydrogenated amorphous carbon, Appl. Phys. Lett. 91 (2007) 1–4. doi:10.1063/1.2794017.

[60] C. Pardanaud, C. Martin, G. Giacometti, N. Mellet, B. Pégourié, P. Roubin, Thermal stability and long term hydrogen/deuterium release from soft to hard amorphous carbon layers analyzed using in-situ Raman spectroscopy. Comparison with Tore Supra deposits, Thin Solid Films. 581 (2015) 92–98. doi:10.1016/j.tsf.2014.10.062.

[61] W.T. Zheng, H. Sjöström, I. Ivanov, K.Z. Xing, E. Broitman, W.R. Salaneck, J.E. Greene, J. -E. Sundgren, Reactive magnetron sputter deposited CN x : Effects of N 2 pressure and growth temperature on film composition, bonding, and microstructure , J. Vac. Sci. Technol. A Vacuum, Surfaces, Film. 14 (1996) 2696–2701. doi:10.1116/1.580190.

[62] G. Liu, Y. Zhou, B. Zhang, K. Gao, L. Qiang, J. Zhang, Monitoring the nanostructure of a hydrogenated fullerene-like film by pulse bias duty cycle, RSC Adv. 6 (2016) 59039–59044. doi:10.1039/C6RA10961F.

[63] K.L. Johnson, Contact Mechanics, (1989). doi:10.1201/b17110-2.

[64] T.Y. Tsui, G.M. Pharr, W.C. Oliver, C.S. Bhatia, R.L. White, S. Anders, A. Anders, I.G. Brown, Nanoindentation and Nanoscratching of Hard Carbon Coatings for Magnetic Disks, MRS Proc. 383 (1995) 447. doi:10.1557/PROC-383-447.

[65] C.A. Charitidis, Nanomechanical and nanotribological properties of carbon-based thin films: A review, Int. J. Refract. Met. Hard Mater. 28 (2010) 51–70. doi:10.1016/j.ijrmhm.2009.08.003.

[66] D.R. McKenzie, R.N. Tarrant, M.M.M. Bilek, T. Ha, J. Zou, W.E. McBride, D.J.H.

Cockayne, N. Fujisawa, M. V. Swain, N.L. James, J.C. Woodard, D.G. McCulloch, Multilayered carbon films for tribological applications, Diam. Relat. Mater. 12 (2003) 178–184. doi:10.1016/S0925-9635(03)00020-7.

[67] B.D. Beake, T.W. Liskiewicz, V.M. Vishnyakov, M.I. Davies, Development of DLC coating architectures for demanding functional surface applications through nano- and micro-mechanical testing, Surf. Coatings Technol. 284 (2015) 334–343. doi:10.1016/j.surfcoat.2015.05.050.

[68] M. Gioti, S. Logothetidis, C. Charitidis, Stress relaxation and stability in thick amorphous carbon films deposited in layer structure, Appl. Phys. Lett. 73 (1998) 184–186. doi:10.1063/1.121749.

[69] C. Mathioudakis, P.C. Kelires, Y. Panagiotatos, P. Patsalas, C. Charitidis, S. Logothetidis, Nanomechanical properties of multilayered amorphous carbon structures, Phys. Rev. B. 65 (2002) 205203. doi:10.1103/PhysRevB.65.205203.

[70] Y. Liu, A. Erdemir, E.I. Meletis, A study of the wear mechanism of diamond-like carbon films, Surf. Coatings Technol. 82 (1996) 48–56. doi:10.1016/0257-8972(95)02623-1.

Figure captions

Figure 1: A simple schematic representing the PIII-based PECVD process.

Figure 2: Deposition rate of single-layered amorphous carbon thin films versus (a) bias voltage, (b) pulse width and (c) frequency are shown.

Figure 3: Fitting a representative Raman spectrum acquired on one of the amorphous carbon films reveals broad graphitic 'G' and disorder-induced 'D' peaks.

Figure 4: Parameters of the G and D Raman spectral lines acquired from single-layered amorphous carbon films as a function of deposition voltage plotted versus (a) I(D)/I(G), (b) D and G positions, and (c) D and G FWHM.

Figure 5: Parameters of the G and D Raman spectral lines acquired on single-layered amorphous carbon films as a function of pulse width plotted versus (a) I(D)/I(G), (b) D and G positions, and (c) D and G FWHM.

Figure 6: Parameters of the G and D Raman spectral lines acquired on single-layered amorphous carbon films as a function of frequency plotted versus (a) I(D)/I(G), (b) D and G positions, and (c) D and G FWHM.

Figure 7: Hardness and elastic modulus of single-layered amorphous carbon thin films versus (a) bias voltage, (b) pulse width and (c) frequency.

Figure 8: H/E and H^3/E^2 of single-layered amorphous carbon thin films versus (a) bias voltage, (b) pulse width and (c) frequency.

Figure 9: (a) Hardness and (b) elastic modulus of multi-layered amorphous carbon films are represented by the data points while the bands show corresponding values for single-layered films. (c) H/E and (d) H^3/E^2 of multi-layered amorphous carbon films are represented by the data points while the bands show corresponding values for single-layered films.

Figure 10: Coefficients of friction for hard/soft multilayer stacks at (a) 6 mN and (b) 10 mN and for hard/intermediate multilayers at (c) 6 mN and (d) 10 mN are shown.

Figure 11: SPM images (scan size 20 × 20 μm^2) of the scratches created at 10 mN peak load on (a) hard, (b) soft and (c) intermediate hardness single-layered thin films. (d) Comparison of scratch profiles of the three samples along the blue line in (a), (b) and (c).

Figure 12: SPM images (scan size 20 × 20 μm^2) of the scratches created at 10 mN peak load on hard/soft multi-layered stacks with interlayer ratio of (a) 1:1, (b) 2:1, (c) 3:1 and (d) 2:2 is shown. (e) Comparison of scratch profiles of the three samples along the blue line shown in (a), (b), (c) and (d).

Figure 13: SPM images (scan size 20 × 20 μm^2) of the scratches created at 10 mN peak load on hard/intermediate multi-layered stacks with interlayer ratio of (a) 1:1, (b) 2:1, and (c) 3:1 is shown. (d) Comparison of scratch profiles of the three samples along the blue line shown in (a), (b), and (c).

Table 1: Table lists all the parameters varied for single-layered coatings.

Figures

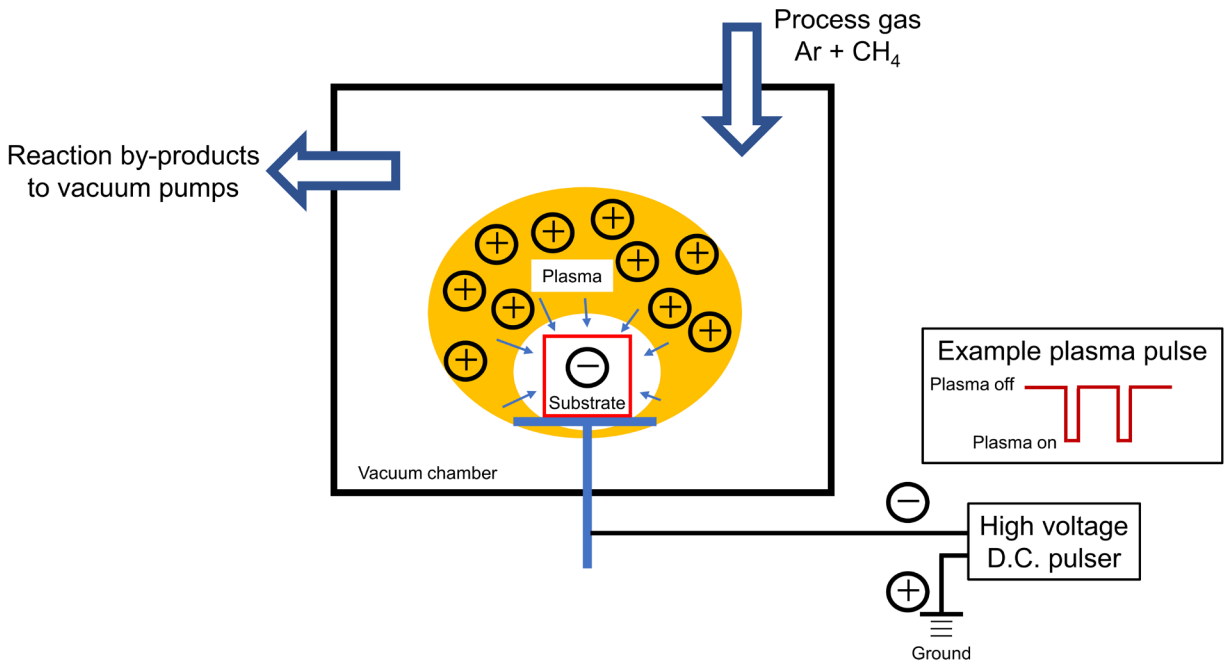

Figure 1

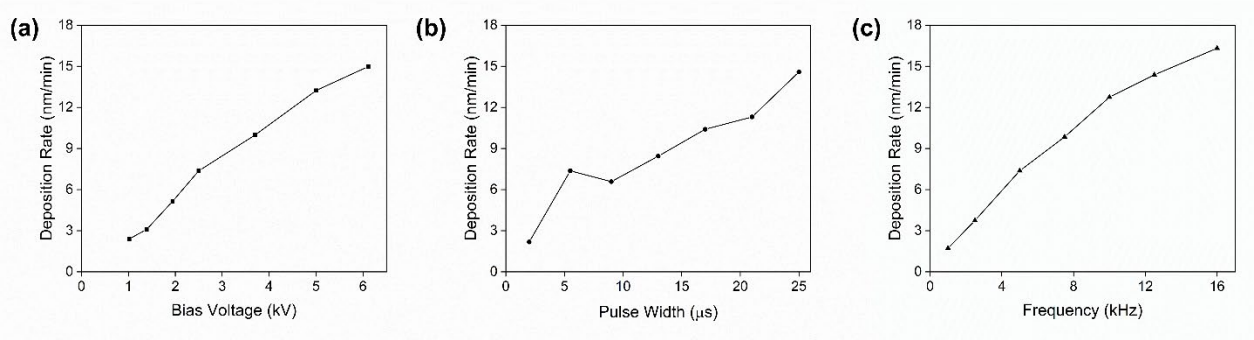
(a)
Deposition Rate (nm/min)
Bias Voltage (kV)
(b)
Deposition Rate (nm/min)
Pulse Width (μs)
(c)
Deposition Rate (nm/min)
Frequency (kHz)

Figure 2

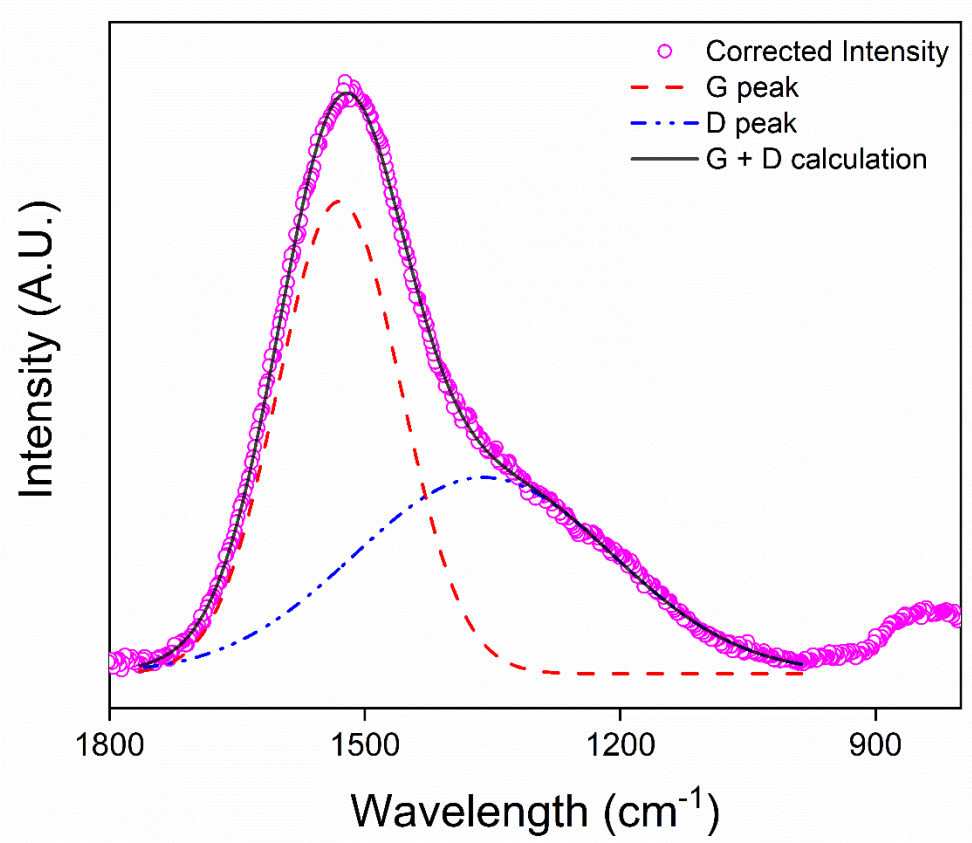
Corrected Intensity
G peak
D peak
G + D calculation
Intensity (A.U.)
1800
1500
1200
900
Wavelength (cm-1)

Figure 3

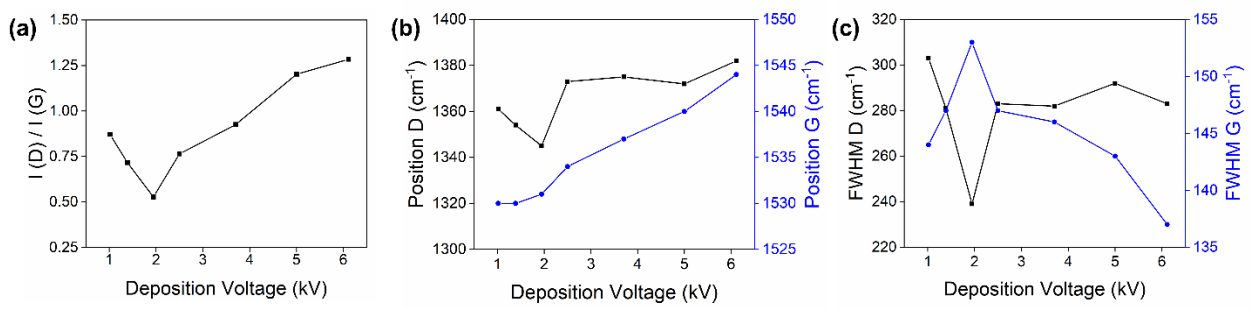
(a)
I (D) / I (G)
Deposition Voltage (kV)
(b)
Position D (cm-1)
Position G (cm-1)
Deposition Voltage (kV)
(c)
FWHM D (cm-1)
FWHM G (cm-1)
Deposition Voltage (kV)

Figure 4

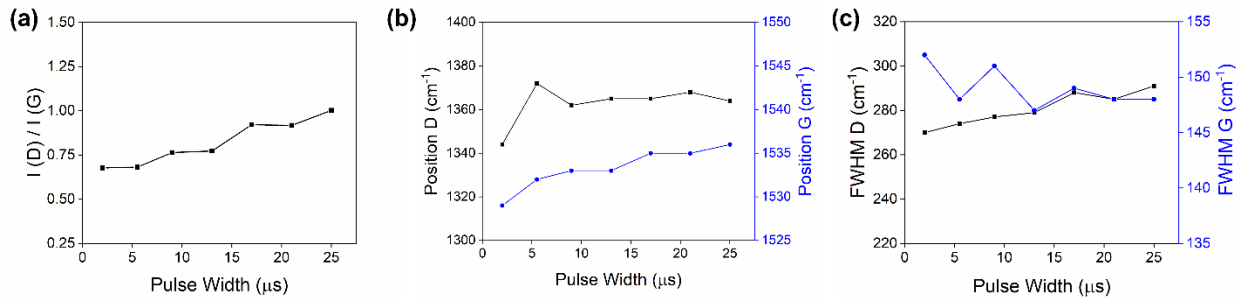
(a)
I (D) / I (G)
Pulse Width (μs)
(b)
Position D (cm-1)
Position G (cm-1)
Pulse Width (μs)
(c)
FWHM D (cm-1)
FWHM G (cm-1)
Pulse Width (μs)

Figure 5

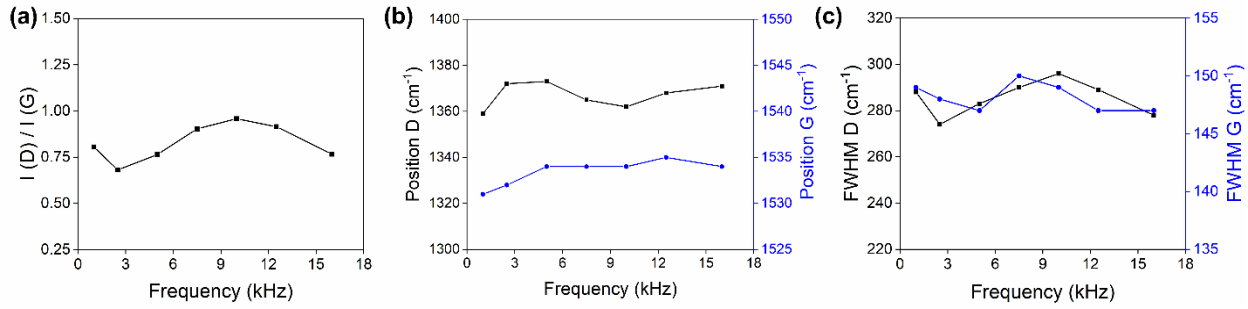
(a)
I (D) / I (G)
Frequency (kHz)
(b)
Position D (cm-1)
Position G (cm-1)
Frequency (kHz)
(c)
FWHM D (cm-1)
FWHM G (cm-1)
Frequency (kHz)

Figure 6

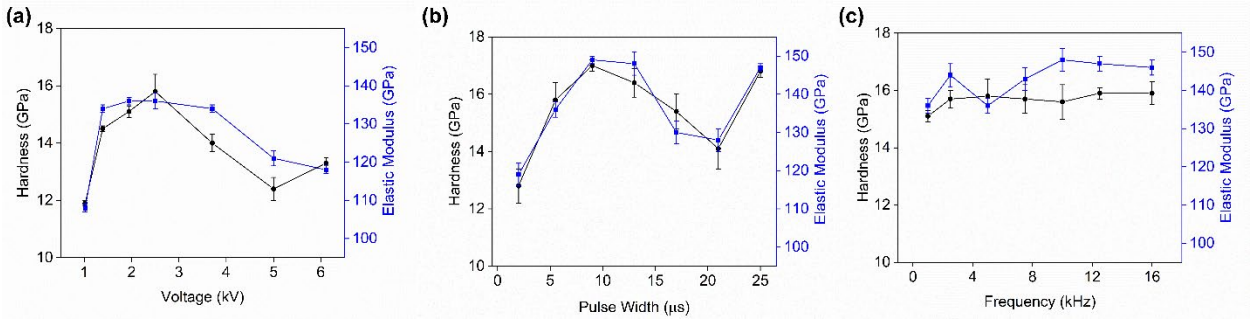
(a)
Hardness (GPa)
Elastic Modulus (GPa)
Voltage (kV)
(b)
Hardness (GPa)
Elastic Modulus (GPa)
Pulse Width (μs)
(c)
Hardness (GPa)
Elastic Modulus (GPa)
Frequency (kHz)

Figure 7

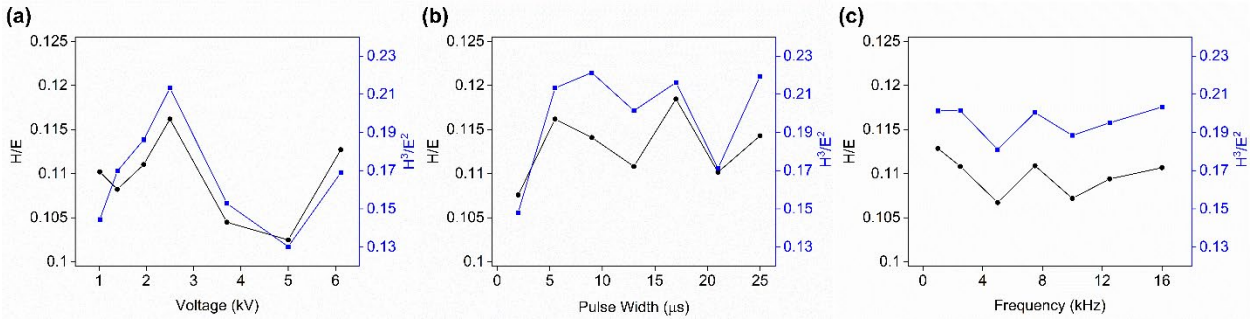

Figure 8

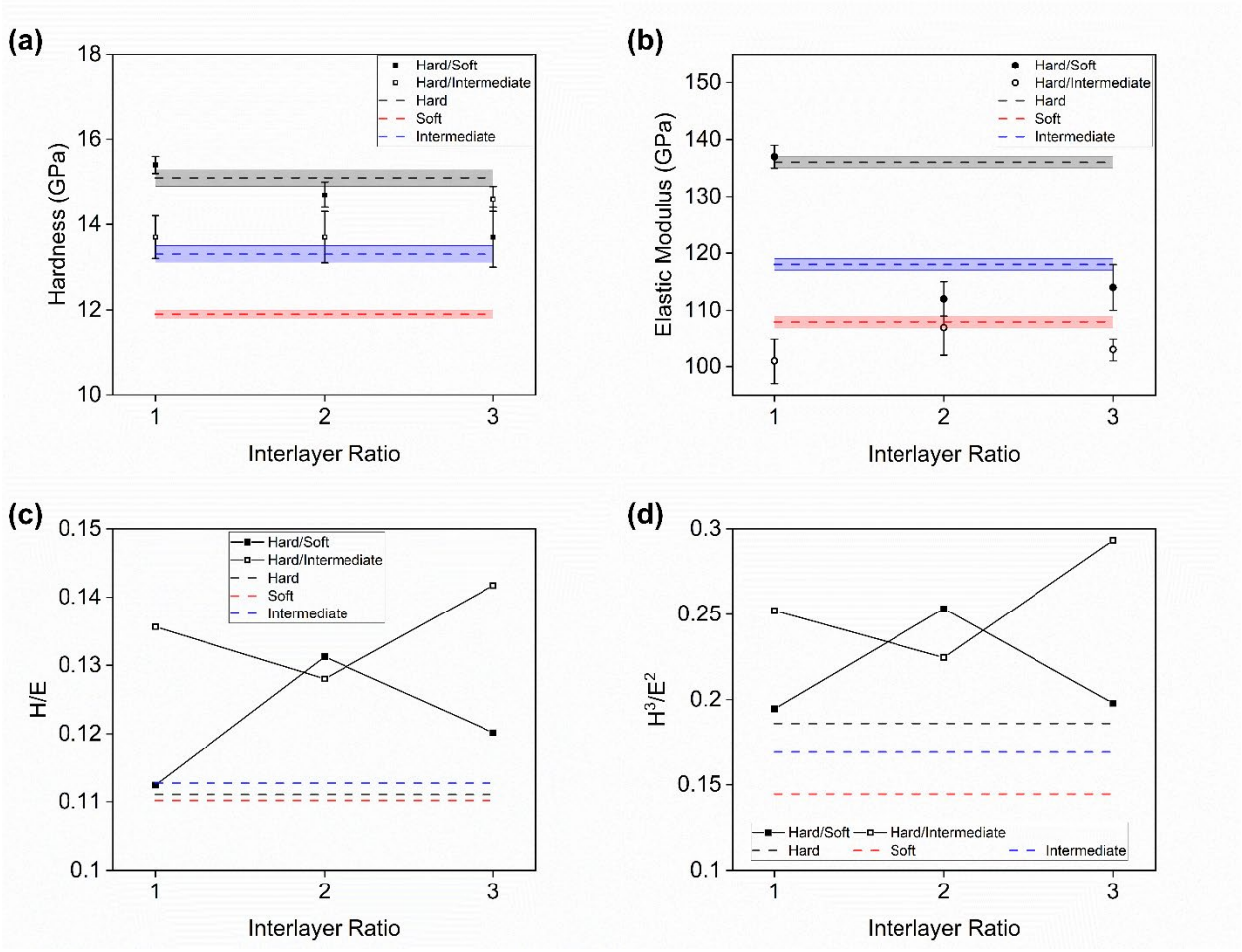
(a)
Hard/Soft
Hard/Intermediate
Hard
Soft
Intermediate
Hardness (GPa)
Interlayer Ratio
(b)
Elastic Modulus (GPa)
(c)
H/E
(d)
H^3/E^2

Figure 9

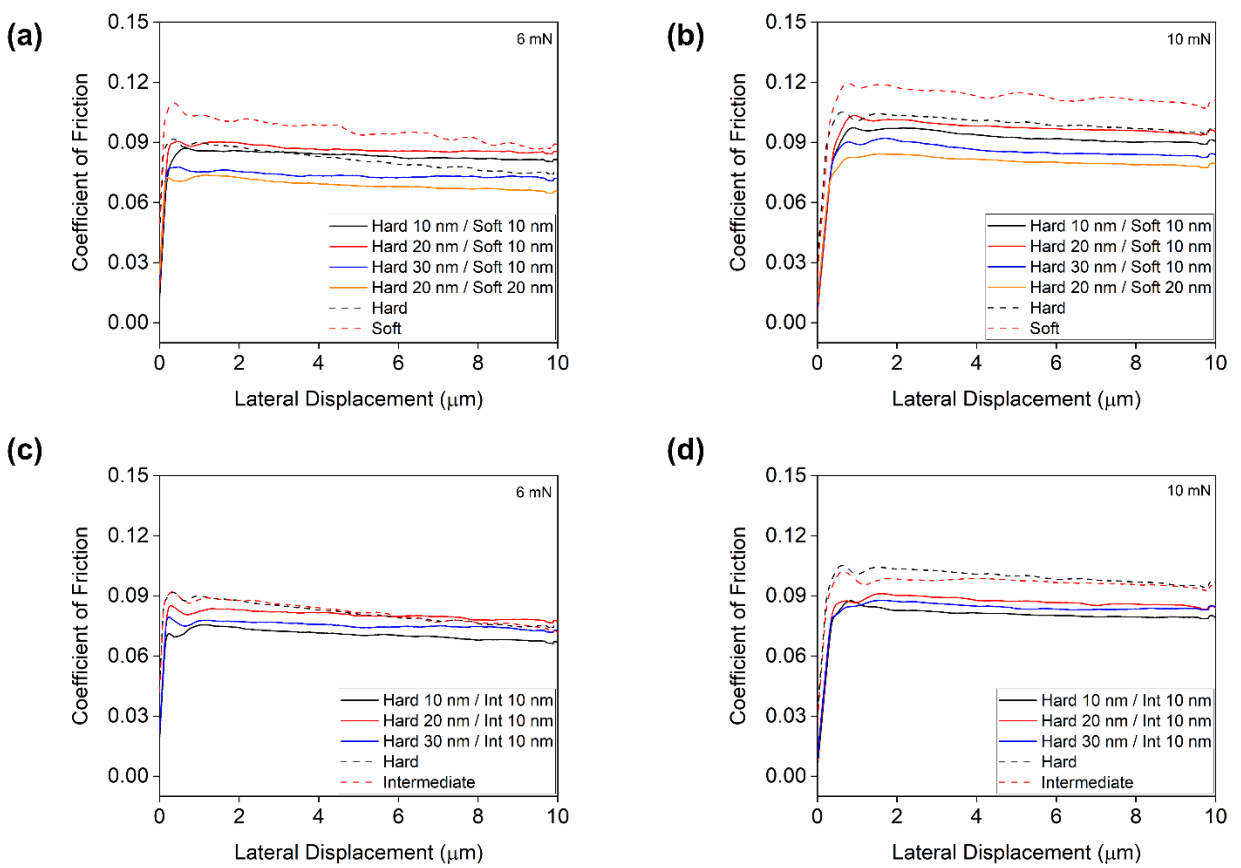
(a)
6 mN
Coefficient of Friction
Lateral Displacement (μm)
Hard 10 nm / Soft 10 nm
Hard 20 nm / Soft 10 nm
Hard 30 nm / Soft 10 nm
Hard 20 nm / Soft 20 nm
Hard
Soft
(b)
10 mN
Coefficient of Friction
Lateral Displacement (μm)
Hard 10 nm / Soft 10 nm
Hard 20 nm / Soft 10 nm
Hard 30 nm / Soft 10 nm
Hard 20 nm / Soft 20 nm
Hard
Soft
(c)
6 mN
Coefficient of Friction
Lateral Displacement (μm)
Hard 10 nm / Int 10 nm
Hard 20 nm / Int 10 nm
Hard 30 nm / Int 10 nm
Hard
Intermediate
(d)
10 mN
Coefficient of Friction
Lateral Displacement (μm)
Hard 10 nm / Int 10 nm
Hard 20 nm / Int 10 nm
Hard 30 nm / Int 10 nm
Hard
Intermediate

Figure 10

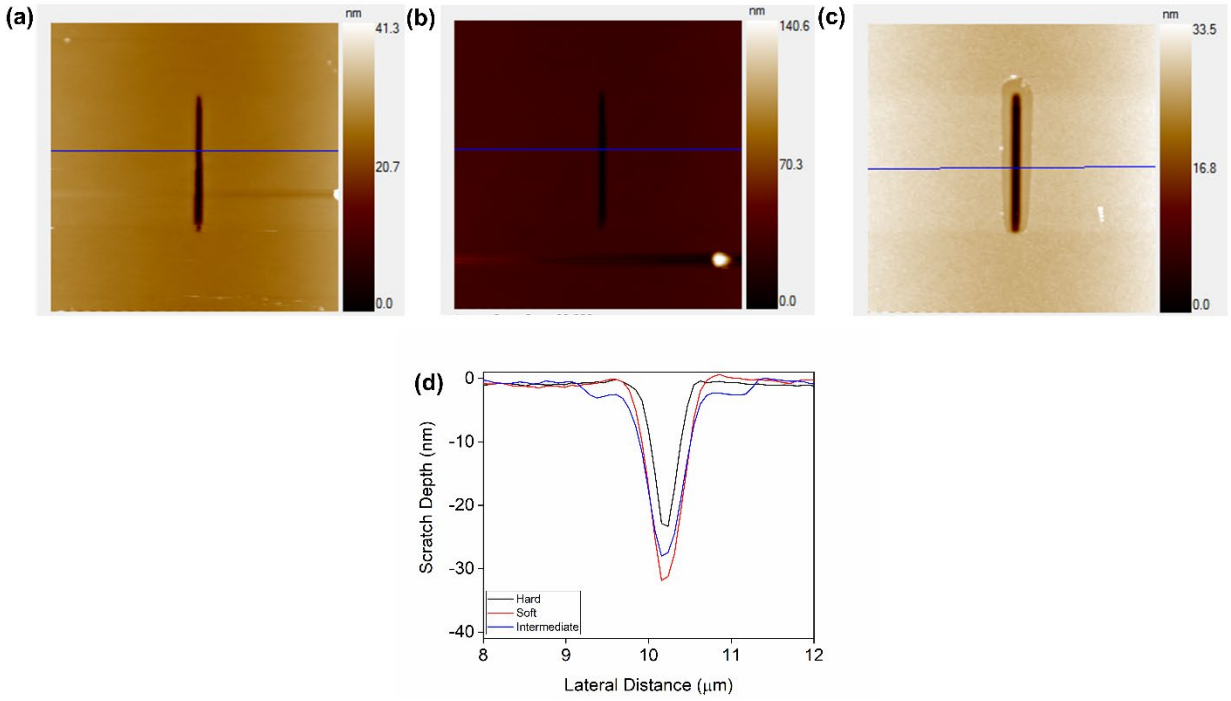
(a)
nm
41.3
20.7
0.0
(b)
nm
140.6
70.3
0.0
(c)
nm
33.5
16.8
0.0
(d)
Scratch Depth (nm)
0
-10
-20
-30
-40
Hard
Soft
Intermediate
8
9
10
11
12
Lateral Distance (μm)

Figure 11

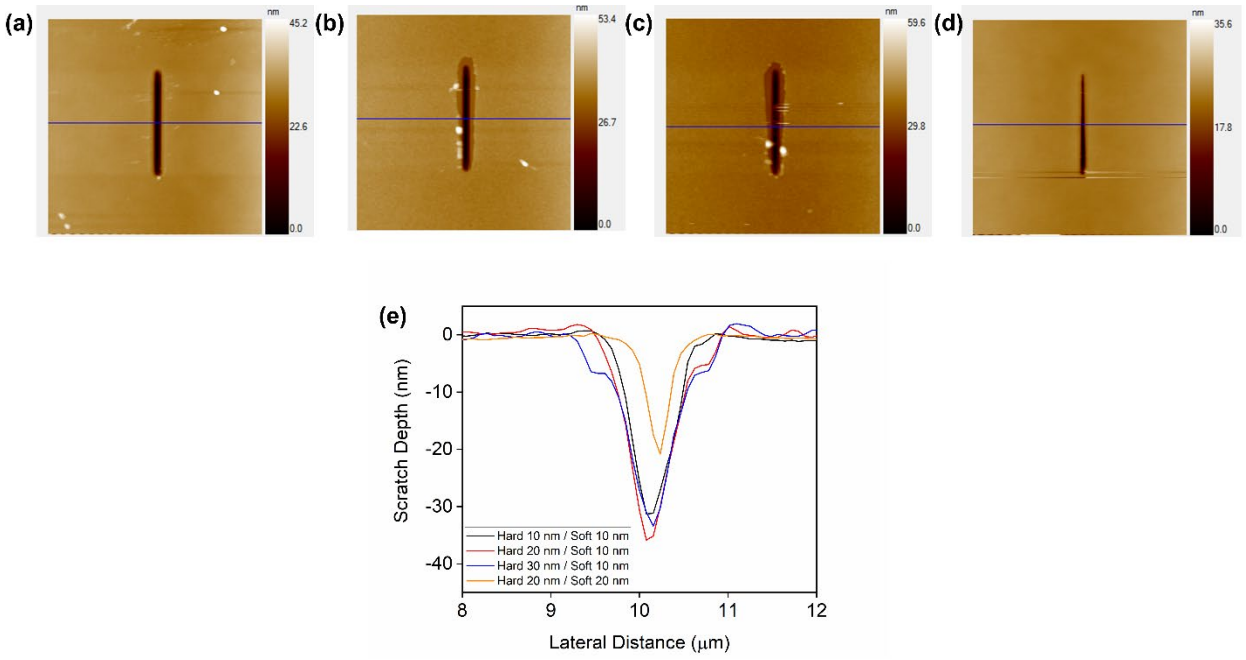
(a)
nm
45.2
22.6
0.0
(b)
nm
53.4
26.7
0.0
(c)
nm
59.6
29.8
0.0
(d)
nm
35.6
17.8
0.0
(e)
Scratch Depth (nm)
0
-10
-20
-30
-40
8
9
10
11
12
Lateral Distance (μm)
Hard 10 nm / Soft 10 nm
Hard 20 nm / Soft 10 nm
Hard 30 nm / Soft 10 nm
Hard 20 nm / Soft 20 nm

Figure 12

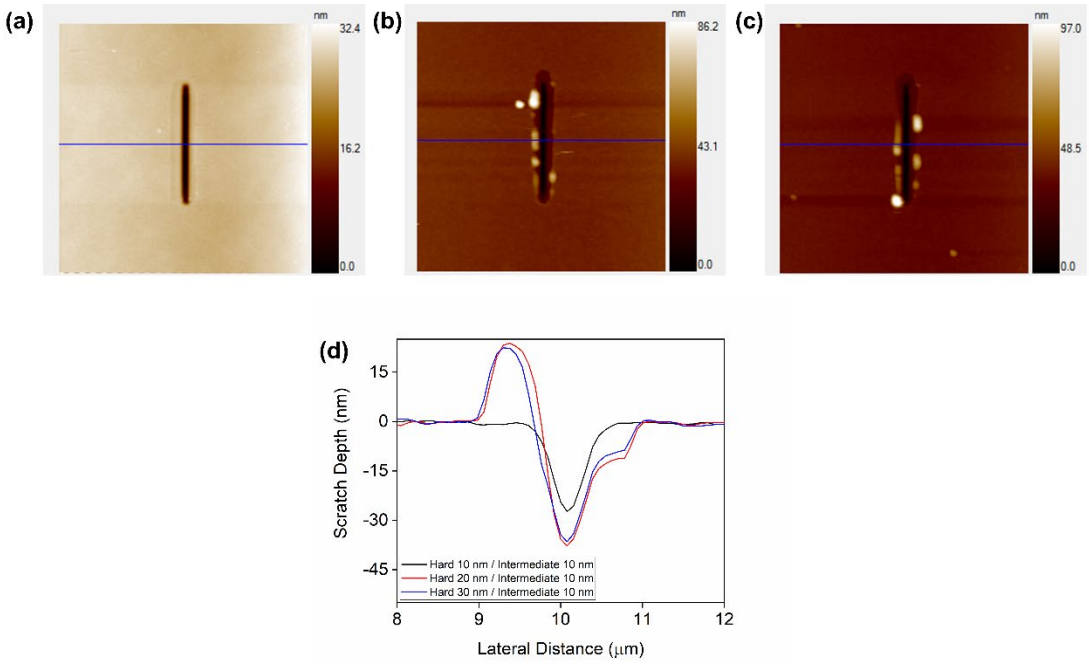
(a)
nm
32.4
16.2
0.0
(b)
nm
86.2
43.1
0.0
(c)
nm
97.0
48.5
0.0
(d)
Scratch Depth (nm)
15
0
-15
-30
-45
8
9
10
11
12
Lateral Distance (μm)
Hard 10 nm / Intermediate 10 nm
Hard 20 nm / Intermediate 10 nm
Hard 30 nm / Intermediate 10 nm

Figure 13